Influence of heterogeneous myelination patterns on axonal conduction and vulnerability to demyelination

Afroditi Talidou[1,2,*] and Jérémie Lefebvre[1,2,3]

[1]Department of Biology, University of Ottawa, Ottawa, ON K1N 6N5, Canada

[2]Krembil Research Institute, University Health Network, Toronto, ON M5T 0S8, Canada

[3]Department of Mathematics, University of Toronto, Toronto, ON M5S 2E4, Canada

[*]Corresponding Author: Afroditi.Talidou@uottawa.ca

Abstract

Axons of the mammalian brain display significant variations in their myelination motifs. Far from being regular and uniform, the distribution patterns of myelin sheaths vary significantly between axons, and across brain areas. To explore the influence of such variability on axonal conduction, we developed an axon model exhibiting myelin distributions mirroring those observed experimentally in different regions of the central nervous system of mice. We also examined how varying myelination patterns predispose axons to failure. Our study shows such variability significantly impacts axonal conduction timing and reliability. Action potential propagation was found to be highly sensitive to the specific arrangement and ordering of myelinated and/or exposed segments along axons, indicating that axonal conduction is non-linear and path-dependent. Furthermore, properties of axonal conduction were found to differ between cortical and callosal axons, influencing their vulnerability to demyelination, while shaping both conduction time and predisposition to failure. Our analysis indicates that callosal axons are particularly sensitive to myelin changes, especially after damage. These findings highlight the crucial role of myelination profiles in brain function and disease.

Introduction

Myelinated axons play a pivotal role in supporting and facilitating the faithful conduction of action potentials (APs). Myelin-forming oligodendrocytes engage in the synthesis of cellular membranes enwrapping axons through a multilamellar spiral configuration [1,2], serving as an effective insulator for the axons and enabling saltatory conduction. Essential for the reliable transit of APs, myelin integrity has been linked to a wide array of brain functions ranging from memory [3,4] and learning [5–7] to executive functions [8–10]. Compromised myelin integrity, resulting from the loss of myelin sheaths and/or oligodendrocytes is closely linked to numerous neurological disorders [11] and neuropsychiatric conditions [12,13].

Individual oligodendrocytes have the capacity to generate multiple myelin sheaths, each of which can exhibit different length and enwraps distinct axons [14]. Numerous investigations delving into the process of myelination have shown that axons manifest highly heterogeneous myelination patterns. Even for axons of the same length and expressing the same net myelin coverage (that is, same percentage of the axon is covered by myelin), myelin sheaths' number, thickness, length and distribution do vary significantly between two given axons as well as across brain areas [15–24]. For instance, cortical and callosal axons possess very distinct myelination motifs: callosal myelin sheath lengths are more variable, compared to cortical axons for which sheath lengths are more similar to each other [14]. These findings challenge the conventional tenet, which commonly portrays sheaths uniformly distributed along axons, disregarding myelination patterns variability. Such variability is the manifestation of the highly plastic and area-specific myelination

process, and the consolidation of signaling pathways by glia: through adaptive myelination and remodelling, myelin sheaths may retract and/or elongate [26–28], altering the lengths of exposed segments/nodes of Ranvier in an axon-specific manner [29, 30]. Variations in myelination patterns is of prime functional significance [15]. Indeed, the distribution of myelin sheath lengths, the molecular constitution of nodes accompanied by variations in the distribution and density of ion and/or leak channels collectively influence axonal conduction and the transit of APs. Myelination motifs notably tune net axonal conduction delays – the temporal interval required for an AP originating at the axon hillock to traverse to the post-synaptic targets – aiming at optimizing the timing of neural signaling thereby supporting neural circuits' function. This is especially salient in the presence of demyelinating diseases: aberrant and/or maladaptive changes such as the lengthening of the nodes of Ranvier, breakdown of the electrically insulating barrier between the myelin sheath and the axonal membrane at the paranodal region, and shrinkage of the sheaths leading to the exposure of K^+ channels in the juctaparanodes, are potential contributors to the modulation of myelinated axon functionality. These changes could, for instance, result in conduction failure or a slowdown of the AP propagation across a diverse spectrum of pathological conditions [31–33].

Understanding the implications of myelin pattern variability would represent an important advancement in our understanding of the tactics employed by glial cells to optimize neural signaling, and in identifying which axons are more vulnerable to injury. For axons with the same lengths and overall myelin coverage, are myelination motifs equivalent? In other words, are they degenerate and do they exhibit redundancy in terms of conduction delay? Are these motifs equally robust to changes in myelin coverage, or are certain motifs more fragile and prone to conduction failure if such coverage was to change? An extensive corpus of scientific literature has developed mathematical models to investigate the propagation of APs along myelinated fibers [34–45]. However, these oftentimes presuppose homogeneous or uniform myelin sheathing interspersed with exceedingly brief nodes of Ranvier, neglecting the highly heterogeneous myelination coverages observed experimentally between axons and brain areas [14, 15]. To challenge this limitation, we built axons exhibiting myelin distribution motifs mirroring those observed experimentally in different regions of the central nervous system of mice. Specifically, we constructed axons displaying myelin sheath length distributions matching those measured from grey (cortical) and white (callosal) matter axons in mice, and characterized the influence of myelination motif variability on AP conduction. This model incorporates variability in myelin sheath lengths, the number of sheaths, and the corresponding lengths and numbers of exposed segments. This enables a comprehensive characterization of the effects of myelin motifs on the reliability of AP conduction and vulnerability of neural signaling to demyelination. We adopted a phenomenological model for the generation and transmission of APs across the exposed segments [44], while also incorporating diffusion to account for the transit of the AP within the myelin sheaths. For each motif

considered, we systematically characterized the reliability of AP propagation timing across axons of different lengths. To quantify reliability, we computed the variability of conduction delays among axons with the same percentage of myelin coverage, referred to herein as PMC. We further measured the incidence of AP conduction failures for each motif, to examine the relationship between myelin distribution and vulnerability to conduction block.

Our analysis revealed that variability in myelin patterns has an important impact on the reliability of axonal conduction. Indeed, AP propagation was significantly impacted by the specific arrangement of myelinated/exposed segments along axons. Conduction delay variability was found to scale with myelin coverage and to vary between cortical and callosal axons, indicating an important sensitivity on the statistics of myelinated and exposed segment lengths. Collectively, these results indicate that AP propagation is a path-dependent process, sensitive to cumulative transitions between and across myelinated and exposed parts of the axon. This was confirmed by the relationship linking conduction delays and lengths of exposed segments, revealing that APs are subjected to bouts of acceleration along the axon and thus, that axonal conduction is a deeply non-linear, path-dependent process. As axonal lengths increase, this was found to represent a determining feature in the faithful transmission of APs: conduction failure rates were also found to depend on myelination patterns. Moreover, the distribution of myelin influences axon vulnerability to demyelination, impacting both conduction time and the rate of conduction failures. Callosal myelination patterns were notably found to exhibit heightened sensitivity to myelin alterations, especially in response to damage. These findings underscore the significant effect of heterogeneous myelination profiles on AP conduction.

Results

Modelling axons with heterogeneous myelin motifs

The primary objective of the present study is to characterize changes in AP conduction caused by realistic and physiologically observed myelination motifs, which are deeply heterogeneous [15]. To accomplish this, we first constructed nerve axon models, incorporating myelin sheath distributions that mirror experimental observations [14]. To this end, we implemented a framework that randomly assigns myelin sheaths to unmyelinated axons of fixed length (Methods). Specifically, we used probabilistic tools to sample myelin sheath lengths, matching those experimentally documented in the cortical and callosal axons of mice [14]. Our approach integrates distinct physiological myelin motifs that faithfully replicate those observed in both grey and white matter, assuming that individual oligodendrocytes predominantly myelinate axons locally,

within the same neural circuits [47]. In vivo studies of cortical and callosal axons in mice reveal considerable variability in the number and length of myelin sheaths formed by individual oligodendrocytes [14]: myelin sheath lengths in callosal axons are more variable compared to those in cortical axons. A schematic of these distinct myelin motifs is depicted in Fig. 1a, alongside statistics of myelin sheath lengths and number for both cortical and callosal axons (Fig. 1b-e).

In order to extend the findings outlined above to axons with differing levels of myelination, we examined five distinct scenarios, each representing varying percentages of myelin coverage (PMC) for a fixed total axonal length (that is, PMC values of 10%, 30%, 50%, 70%, 90%). Variations in PMC reflect the number of sheaths per axon [18]. For our nerve axon models, the relative frequency of the number of myelin sheaths in cortical and callosal axons is shown in Fig. 1b, c. When considering an axon of fixed length, any modifications in the number or lengths of myelin sheaths inevitably influence the corresponding number or lengths of exposed segments (that is, the unmyelinated ones). By construction, both cortical and callosal axons exhibit a high density of short exposed segments (Fig. 1e), reminiscent of nodes of Ranvier [29].

To enable meaningful comparisons between these myelination motifs and their respective influence on AP propagation, we made the assumption that, aside from sheath distribution patterns, axons possess identical properties: total axonal length (L), radius (a) and myelin sheath thickness (determined by the g-ratio) were assumed to be identical. Unless explicitly stated otherwise, other parameters, such as membrane capacitance and membrane resistance, were also held constant (included in Table 1).

We modelled the propagation of APs along these axons using the cable theory [46], adapted to account for heterogeneous myelination motifs. To simulate spike generation and conduction within the exposed segments, we used a spike-conducting integrate-and-fire model [44]. The rapid spread of APs along myelinated axons was replicated assuming a pure diffusion model. The resulting system of equations is supplemented by additional conditions that account for the current flow at the paranodal junctions, where the membrane potential transitions from myelinated to exposed axonal segments, and vice versa (Methods). Fig. 2a illustrates the slow and fast conduction along an exposed and a myelinated segment, respectively. Under the premise that all other parameters remain unchanged, our model captures the significant influence of myelination patterns on AP propagation. A representative example illustrating the differences in AP conduction between a cortical and a callosal axon is presented in Fig. 2b-e. Despite having identical lengths and PMC, the net conduction velocity (CV) and delay of APs differ between these two axons. This discrepancy is influenced by the distribution, number, and length of myelin sheaths and exposed segments.

Heterogeneity of myelin sheath distribution impacts AP conduction time

In the light of the manifest heterogeneity in myelination motifs observed experimentally [14], a natural question arises as to how the distribution of sheaths influences the reliability, propagation and efficacy of AP conduction. Given the distinct propagation patterns observed (see Fig. 2), the time required for an AP to propagate along axons will likely depend on the distributions of myelinated and exposed segments. To quantify this path dependence, we computed spike timing in each segment, indicating the time at which the AP crosses the threshold values at both the beginning and end of each segment. The absolute difference between these two times corresponds to the delay for the AP to traverse the segment. Summing up these delays across segments spanning the length of an axon yields the net axonal conduction delay τ. The associated net axonal CV v was determined by evaluating the ratio of the total axonal length L to the conduction delay τ (Methods).

For each value of PMC and fixed axon length, we computed the net conduction delays and the corresponding net CVs based on a cohort of 500 independent realizations of axons with identical statistical properties. The lengths and/or number of myelin segments along those axons were randomly sampled from either cortical or callosal myelin distributions (see Fig. 1b-e). Net conduction delays were expectedly found to decrease with the incremental addition of myelin (Fig. 3a), while the net CVs increased with PMC values (Fig. 3b). The mean conduction delay and CV were both found to be identical between cortical and callosal axons (Fig. 3e). Of particular significance, however, is the dispersion in conduction delays, indicative of variability in AP propagation between and even within cortical and callosal myelination motifs. To quantify this variability, we computed the standard deviation (std) of the net conduction delay. The net conduction delay variability was found to be approximately twofold larger for callosal axons compared to cortical axons, a trend preserved for all PMC levels considered (Fig. 3c), despite being controlled for length, PMC, and all other physiological parameters (see Methods). Net conduction delay variability is negatively correlated with PMC: as PMC increases, the dispersion of conduction delays decreases. The associated net CV exhibited markedly lower variability, a trend consistently observed across both myelination motifs (Fig. 3d). This lower variability results directly from the non-linear relationship between conduction delay and velocity. Taken together, these results confirm that myelination patterns significantly influence AP propagation variability, indicating that axonal conduction is a path-dependent process, sensitive to the cumulative effect of transitions between and across myelinated and exposed parts of the axon.

The consequences of heterogeneous myelin motifs are not limited to issues of reliability. Our analysis indicates that faithful AP transmission (that is, conduction success or failure) is also contingent on myelin distribution. Conduction failure arises from factors such as high stimulation frequency and/or diminished

capacity of membrane potentials to depolarize in regions deprived of myelin [48]. This has important functional implications, such as failing to elicit the depolarization of postsynaptic cells. In our model, such conduction failures occur when membrane potential fluctuations fail to reach the paranodal junction while traversing longer exposed segments. Consequently, the AP amplitude drops below the threshold required for the spike initiation (Fig. 3g). An illustration of successful conduction is portrayed in Fig. 3f, where the AP amplitude maintains supra-threshold values throughout the entire axon. By calculating the rate of conduction failures (Methods), we identified that both cortical and callosal axons displayed systematic failure in cases of weak myelination (PMC=10%, Fig. 3h), primarily attributable to the presence of long exposed segments. These segments provide more opportunities for ion leakage across the axonal membrane, contributing, among other factors, to the gradual loss of depolarization necessary for AP propagation. A considerably lower rate of conduction failures was observed in axons exhibiting higher degrees of myelination, with myelination patterns inherent to callosal axons showing slightly higher susceptibility to failures. In summary, our findings suggest that axons in grey matter may demonstrate heightened resilience to changes in PMC.

Effects of myelination patterns on axonal conduction across spatial scales

One proposed role of myelination is to compensate for increasing physical distances separating neurons, notably those that arise during development [49]. Nevertheless, a fundamental question remains: do heterogeneous myelination motifs impact axonal conduction evenly along neuronal axons of different lengths? To address this question, we conducted additional numerical simulations covering a range of axonal lengths spanning three orders of magnitude (from 1 mm to 100 mm).

We computed the net axonal conduction delays and CVs in each case, first restricting our analysis to axons that successfully transmitted the signals (that is, excluding axons resulting in AP conduction failure). Our simulations revealed a greater sensitivity of longer axons to myelin changes in both cortical and callosal myelin motifs. These translated in increased AP conduction time variability. Fig. 4a shows that, for a set PMC, mean conduction delays expectedly increase with axonal lengths for both cortical and callosal myelin motifs. However, the behaviour of mean CVs is more complex. The shortest axons examined (i.e., $1\,mm$) exhibited significantly higher CVs, primarily attributed to the effect of current reflection occurring at the ends of these axons [50]. This resulted in enhanced conduction over shorter distances (Fig. 4b). Such boundary effects gradually vanish for longer axons in both cortical and/or callosal motifs resulting in lower mean CVs. As axonal lengths increase, the slope of the mean conduction delay versus velocity curves steepens (Fig. 4c). This observation suggests that, for longer axons (i.e., $10 - 100\,mm$) and for the same PMC, APs propagate at approximately the same CV. We further quantified reliability by computing conduction delay

variability resulting from cortical and callosal myelination motifs. As can be seen in Fig. 4d, variability of net conduction delays increases with axonal length - suggesting longer axons are less reliable than shorter ones and more sensitive to variations in myelin distributions. This variability was also found to be more pronounced among callosal axons. This contrasts with the trend seen in CV: CVs were found to be more variable in shorter axons, due to the aforementioned effect of current reflection (Fig. 4e).

We then turned our attention to how myelination patterns and axonal lengths influence predisposition to conduction failure. As can be seen in Fig. 4f, conduction failure rates increased with axonal lengths evenly between cortical and callosal axons, suggesting that myelination patterns do not influence the predisposition to conduction failure. These findings underscore the effect of myelination patterns in regulating conduction timing across varying axonal lengths.

AP propagation is non-linear along heterogeneously myelinated axons

The results displayed in Figs. 3-4 confirm a strong dependence of axonal conduction delay and CV on myelin distribution. Indeed, even when controlled for differences in PMC and/or length, conduction delays exhibit important variability within and between cortical and callosal axons. These results imply that AP conduction delays do not solely rely on PMC or total length of the axon, but are dependent on the distribution, ordering and lengths of myelinated and/or exposed segments. Such path-dependence is supported by our mathematical analysis (Methods), which indicates that AP conduction is a non-linear process in which APs are subjected to bouts of acceleration along exposed segments. This acceleration causes the CV to scale non-linearly with length in the presence of heterogeneous motifs in which exposed segment lengths vary. The existence of this acceleration is confirmed in Fig. 5, in which one can see the logarithmic relationship between AP conduction delay and segment length. These results suggest that AP conduction is a path-dependent process, sensitive to cumulative transitions between and across myelinated and exposed parts of the axon - and hence a dependence on myelination pattern. If CVs remained constant along exposed segments (that is, there is no acceleration), conduction delays would scale linearly with their length, and conduction delay variability resulting from changes in myelin distribution would vanish (Methods). These results further imply that variability in conduction delay is reduced whenever the number of exposed segments increases. Indeed, as the lengths of exposed segments decrease and become infinitesimal, as commonly assumed for nodes of Ranvier in various computational studies (for example, [29,40]), the non-linear behaviour portrayed in Fig. 5 disappears, and conduction delay variability ceases to occur. These findings shed new light on the results presented in Figs. 3-4, revealing that cortical axons exhibit smaller variability compared to callosal axons due to the disparity in their myelin distribution. Indeed, Fig. 5 reveals that callosal axons display

a more salient non-linearity when compared to cortical axons: acceleration is hence more pronounced in callosal axons. This is directly linked to statistical differences in exposed segment lengths between cortical and callosal axons (see Fig. 1). It is interesting to conjecture on the functional implications of this non-linearity and consider whether myelin distribution also influences their vulnerability to demyelination.

Vulnerability of myelination patterns to demyelination

Upon the onset of demyelination, the integrity of myelin sheaths becomes compromised or completely breaks down, subsequently causing disruptions in the transmission of nerve impulses [48]. Such demyelination results from the loss of myelin sheaths and/or oligodendrocytes, and occurs in numerous neurological [11] and neuropsychiatric [12, 13] disorders. We next examined how cortical and callosal myelination patterns were impacted by gradual demyelination, and quantified their resulting predisposition to conduction failure. We modelled such demyelination by systematically reducing the number of myelin sheaths while replacing the damaged segments with excitable ones exhibiting lower excitability to account for a pathological decrease in ion channel density (Methods). We modelled demyelination-induced changes in excitability by altering the depolarization threshold for those segments, ranging from −10 to −50 mV, all of which exceed the threshold value at the unaffected exposed segments/nodes of Ranvier (−60.2 mV). A schematic illustration portraying the demyelination process described above is presented in Fig. 6a. We induce demyelination in cortical and callosal axons, each with a length of 10 mm, and initial PMC set at 90%. The reduction in the number of myelin sheaths naturally affects the PMC in the damaged axons. The pie charts in Fig. 6b illustrate the mean value of the percentages of exposed, myelinated and demyelinated space along axons for three cases of myelin damage. Along healthy cortical and callosal axons, statistics for the number and/or length of myelin sheaths differ. Hence, statistics for demyelinated segments also differ: callosal axons exhibit lower number of demyelinated segments, for the same overall percentage of damage (Fig. 6c). Given those differences, is AP conduction along cortical and callosal axons equally vulnerable to demyelination? To measure vulnerability we computed the rate of axonal conduction failures for various AP threshold values and as myelin damage progresses. We observed that callosal axons are more vulnerable to demyelination, compared to cortical ones, exhibiting much higher rates of conduction failure (Fig. 6d). Moreover, for both cortical and callosal axons, conduction failures expectedly become more prominent as the excitability of demyelinated segments decreases (i.e., depolarization threshold increase, reflecting lower ion channel density). Conversely, Fig. 6d also shows that increase in axonal excitability – resulting from adaptive changes in ion channel density, for instance – may compensate for, and decrease the predisposition to, demyelination-induced conduction failure. Failure rates are the consequence of increased variability in AP waveform, resulting from myelin

damage. Closer examination of demyelinated sheath lengths in Fig. 6e indicates that conduction failures occur more often when long sheaths experience damage/demyelination. In contrast, axons that succeed at conducting APs in spite of such damage are characterized by short demyelinating sheaths. We note that this could be attributable to the fact that larger portions of the axon become exposed, a result compatible with results depicted in Fig. 3f. We then examined how demyelination affected the conduction delays along axons that did not experience failure in spite of suffering extensive damage. Figure 6f indicates changes in mean conduction delay compared to healthy axons (Fig. 3c), a trend observed for both cortical and callosal patterns. Intriguingly, we observed faster conduction with increased damage in some axons, suggesting a demyelination-induced increase in net axonal CV. This counter-intuitive result could be attributed to multiple mechanisms pertaining to localized changes in axonal excitability [59], such as AP induction, spontaneous firing and after discharges. Nonetheless, these results suggest that in addition to failure, demyelination predisposes AP to time jitter by influencing their conduction time towards their postsynaptic targets. To better understand this effect, we focused on axons exhibiting successful conduction (in both heathly and damaged axons), and measured time fluctuations in the peak membrane potential (i.e. states of maximal depolarization) as APs traverse the axons (Fig. 6g). Our analysis shows that APs experience significant modulation when traversing damaged axons (Fig. 6g-e): the peak membrane potential varies considerably compared to healthy axons, where peak membrane potential remains relatively constant throughout. Such variability predisposes damaged axons to conduction block: demyelination-induced modulation in AP amplitude could fail to meet the depolarization threshold. As such, fluctuations in AP amplitude can be seen as interrogating both local excitability and myelin coverage, predisposing the axon to failure whenever the AP encounters long demyelinated segments (Fig. 6e-f). We highlight that this is another salient - and potentially pathological - manifestation of the highly nonlinear, path-dependent nature of axonal conduction along axons exhibiting heterogeneous myelin patterns.

Discussion

Numerous experimental studies have revealed that mammalian axons display a wide variety of myelination patterns. Significant variation in the number, thickness, length, and distribution of myelin sheaths between different axons and across various brain regions is the norm rather than the exception [15–24]. Notably, axons in the cortex and corpus callosum of mice exhibit markedly different motifs: cortical myelin sheaths display less variation compared to callosal ones [14, 15]. This manifest variability is at odds with numerous computational studies [34–45], considering the axon as a cable with uniform myelin sheathing interspersed with exceedingly brief nodes of Ranvier. Motivated by the commanding influence of myelin

on AP propagation, and its well-documented consequence on brain function [3–10], we here explored the influence of heterogeneous myelination patterns on axonal conduction reliability and predisposition to failure. Specifically, we developed a mathematical model of excitable axons displaying myelination patterns mirroring those observed experimentally in the cortex and corpus callosum of mice [14]. In this work, we introduced a mathematical model providing the flexibility to analyze the propagation of APs along single axons with more physiological myelin patterns. We systematically examined how such myelination motifs influence AP conduction delays and CVs as well as vulnerability to failure in both healthy axons and those subjected to demyelination.

Our analysis revealed that variability in myelin patterns has an important impact on the reliability of axonal conduction. Indeed, axonal conduction was found to be path-dependent, sensitive to myelin distribution patterns through the cumulative effect of AP propagating across myelinated and/or exposed segments of various lengths. Variability in conduction delays correlates inversely with myelin coverage and differed between callosal and cortical axons. We further explored how this influenced axons of different lengths: variability in AP conduction was found to increase with axon length, and to be more prominent in callosal axons compared to cortical axons. Likelihood of conduction failures was found to be influenced by PMC, axonal lengths and myelination patterns. We thus emulated demyelinating damage by selectively removing sheaths and quantifying resulting changes in AP conduction. Callosal axons, in particular, were found to display a greater sensitivity to demyelination, exhibiting increased failure rates compared to cortical axons.

Collectively, these results suggest that motifs of myelination play an important functional role by influencing the timing and reliability of neural signaling. The reported sensitivity and path-dependence of axonal conduction delays and CVs on myelin distribution highlights the functional role of glia in orchestrating neural communication and securing brain function [3–10, 25, 26]. Indeed, variations in myelin coverage and pattern is the result of highly plastic processes such as adaptive myelination and myelin remodelling [26–30]. Our results make a strong case that even subtle changes resulting from impaired and/or inadequate myelination may result in significant consequences on axonal conduction delay/CV, and predispose otherwise healthy axons to conduction failure. In the light of our results, it remains unclear how glia optimize myelin coverage to stabilize axonal conduction.

Our results identify an important difference between myelination motifs in the cortex and corpus callosum, and their vulnerability to demyelination. This difference echoes a long-standing conundrum in the literature pertaining to the pathological manifestation, consequences and clinical relevance of grey versus white matter lesions observed across multiple sclerosis stages [62–64]. It is interesting to conjecture that variations in myelination patterns and resulting differences in vulnerability to demyelinating damage reported here may

be involved in MS progression. For instance, the relatively higher resilience of cortical axons to damage (cf. Fig. 6) suggests that grey matter could involved in later stages of the disease compared to white matter axons. Further research is required to delineate the respective contributions of grey and white matter axons in MS severity and progression.

While providing valuable insights, our study nonetheless faces limitations. First, we used a model that overlooks detailed ion channel dynamics. The distribution of ion channels along exposed segments and the potential variation in their density within a given axon are open questions that warrant further investigation. Second, we introduced variability exclusively to the longitudinal lengths of myelin sheaths and exposed segments, while keeping the axon radius constant and refraining from altering the thickness of the myelin. Introducing other sources of variability such as the g-ratio and/or axon diameter [60] would certainly increase the scope of our conclusions. Thirdly, in characterizing the relationship between myelination motifs and variability in axonal conduction delay, we used a phenomenological approach grounded in axonal geometry. A more precise mathematical approach, incorporating additional boundary conditions at the paranodal junctions, would significantly enhance the physiological relevance of our model, and allow us to better understand the role played by paradonal junctions in AP conduction.

Figures

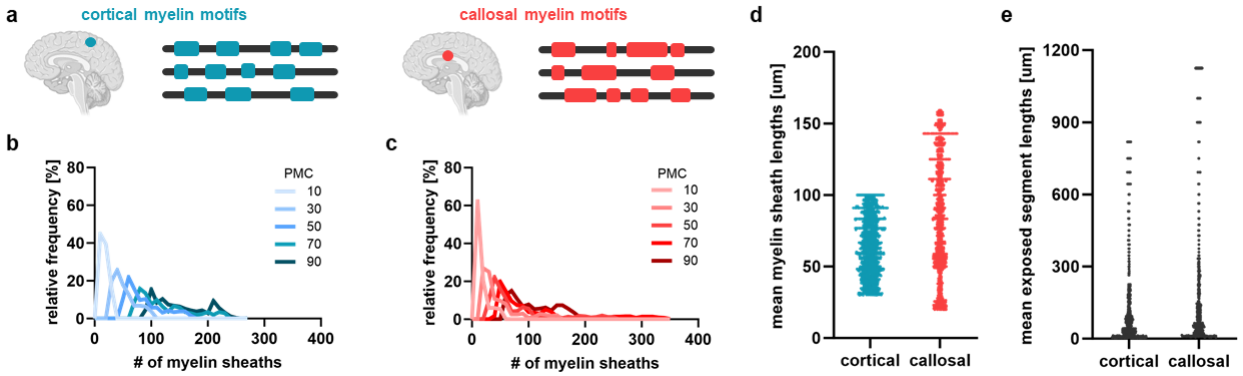

Figure 1. Modelling myelination motifs in grey and white matter. a, Schematic of heterogeneous myelination motifs along individual axons in two different brain regions: in the cerebral cortex (blue) and corpus callosum (red). **b,** Frequency distributions of the number of myelin sheaths for PMC $= 10, 30, 50, 70$ and 90 for axons following the cortical myelin motifs. **c,** Frequency distributions of the number of myelin sheaths for axons following the callosal myelin motifs. **d,** Scatter plot of the mean value of myelin sheath lengths for cortical and callosal axons for all cases of PMC considered. **e,** Scatter plot of the mean value of exposed segment lengths for all cases of PMC and for both cortical and callosal myelin motifs. The geometrical parameters of the axons used are: axonal length = $10\,mm$, radius = $2\,\mu m$ and g-ratio = 0.6. The biophysical parameter values used are given in Table 1. The results shown are for $K = 500$ independent trials.

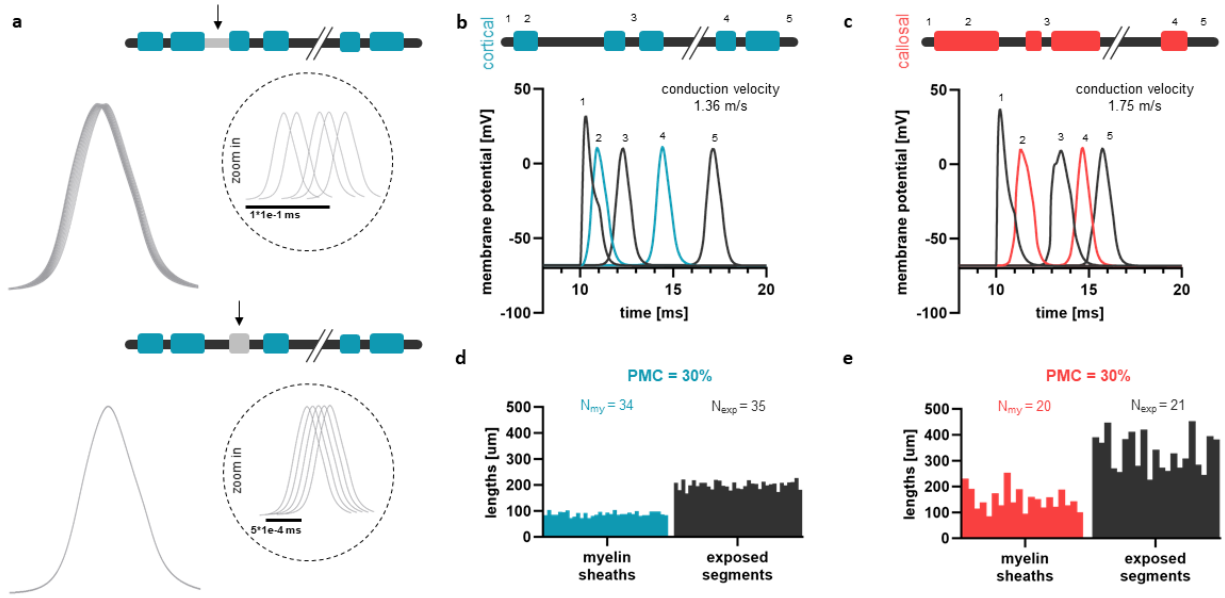

Figure 2. Myelination motifs impact AP propagation. a, Schematic of a cable (dark grey) ensheathed by myelin (blue rectangles). The pulses represent the propagation of the AP as a function of time along an exposed segment (spikes drawn at multiple locations at the segment depicted by light grey – top panel) and along a myelin sheath (spikes developing promptly – bottom panel). Zoom in circles show how fast the AP is travelling at the particular segments. **b, c,** Representative examples of the AP propagation along a cortical (blue) and a callosal (red) axon. Snapshots of the APs at different parts of the axons show the disparity between net conduction velocities and delays. The illustrative patterns of myelination at the top correspond to the distributions of panels d and e. **d,** Distributions of myelinated and exposed segment lengths for a cortical axon with fixed PMC = 30%. The number of myelinated segments is N_{my} = 34 and of the exposed segments is N_{exp} = 35. **e,** Distributions of myelinated and exposed segment lengths for a callosal axon with fixed PMC = 30%. The number of myelinated segments is N_{my} = 20 and of the exposed is N_{exp} = 21. Geometrical parameters used are: axon length = 10 mm, cable radius = 2 μm and g-ratio = 0.6.

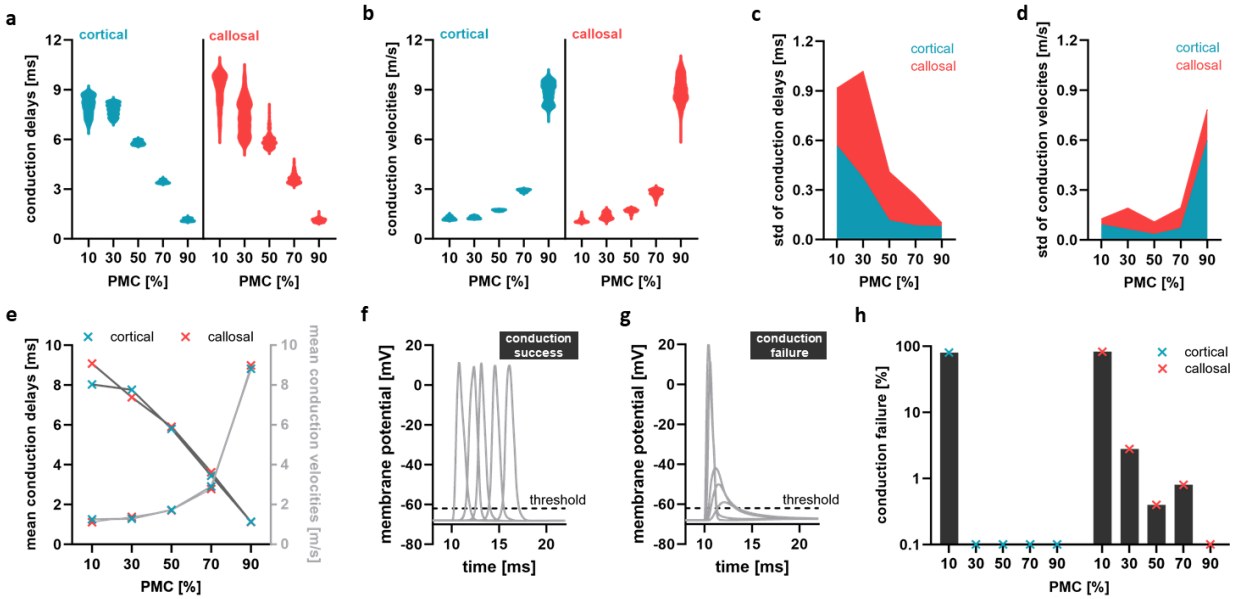

Figure 3. Axonal conduction variability as a result of heterogeneous myelination along single axons. a, Distribution of axonal conduction delays (measured in *ms*) plotted for different myelin coverage showing the differences between cortical and callosal myelin profiles. **b,** Distributions of the corresponding axonal CVs (measured in m/s) for the five cases of PMC values. **c,** Plotted is the standard deviation (std) of axonal conduction delays for cortical and callosal myelin motifs. **d,** Standard deviation of the corresponding axonal CVs for cortical and callosal myelin motifs. **e,** Mean values of axonal conduction delays (dark grey) and CVs (light grey) as a function of PMC. **f,** Snapshots of an AP propagation with respect to time. The peak of the AP remains above the threshold at all times indicating that the AP reaches successfully the end-point of the axon. **g,** Snapshots of an AP propagation that fails to arrive at the axonal end-point. The peak of the AP crosses the threshold and remains below that afterwards. **h,** Rate of conduction failures, that is, the number of failures over the total number of trials, plotted for each PMC.

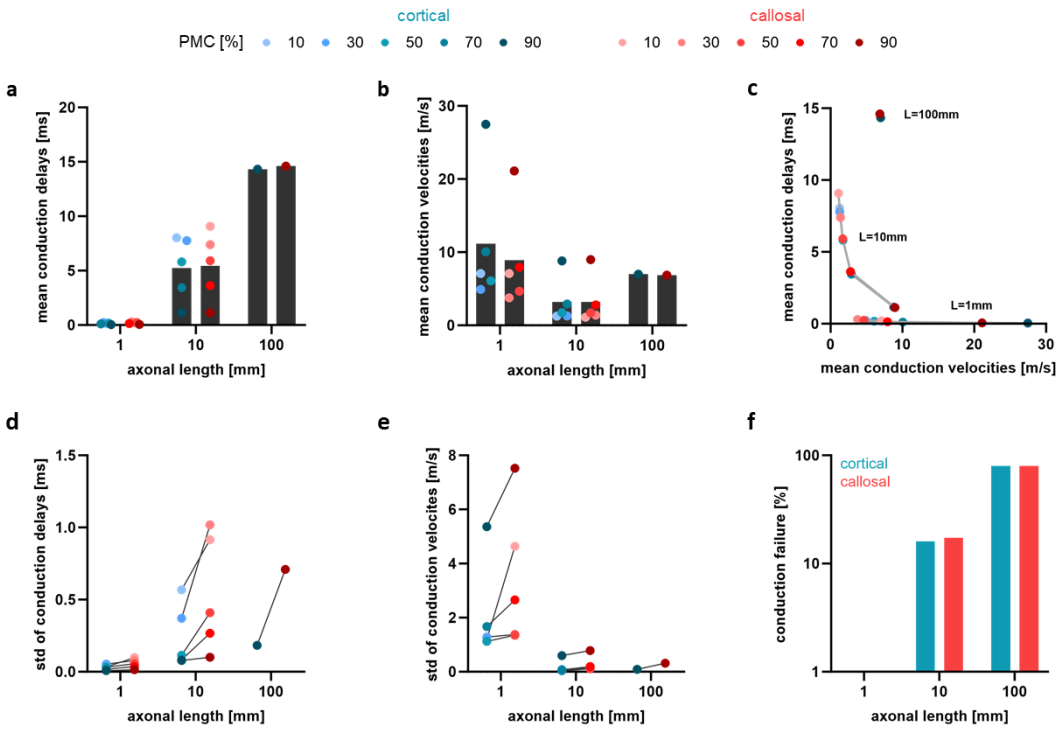

Figure 4. Axonal lengths modulate conduction properties. a, Mean conduction delays of both cortical (blue circles) and callosal (red circles) axons positively scale with axonal length. The intensity of the colour corresponds to the PMC value, where lighter to darker shades indicate weak to strong myelin coverage, respectively. **b,** Corresponding mean CVs as a function of axonal length. The mean CVs negatively scale with length: as axonal lengths increase, the mean CVs decrease. **c,** Mean conduction delays plotted as a function of mean CVs for cortical and callosal axons. The curve of the rate of change slants downward faster as axonal lengths increase. **d,** Standard deviation of conduction delays against axonal lengths. For short axons with a length of 1 mm, the dispersion of conduction delays is minimal. Across all axonal lengths and PMC, the values associated with callosal axons consistently exceeded those of cortical axons. **e,** Standard deviation of CVs against axonal lengths. Short axons have fewer myelin sheaths, and when combined with boundary effects, this could lead to an increased jitter of CVs. This effect diminishes as axonal lengths increase. **f,** Rate of conduction failures as a function of axonal lengths. Values collectively plotted for all cases of PMC.

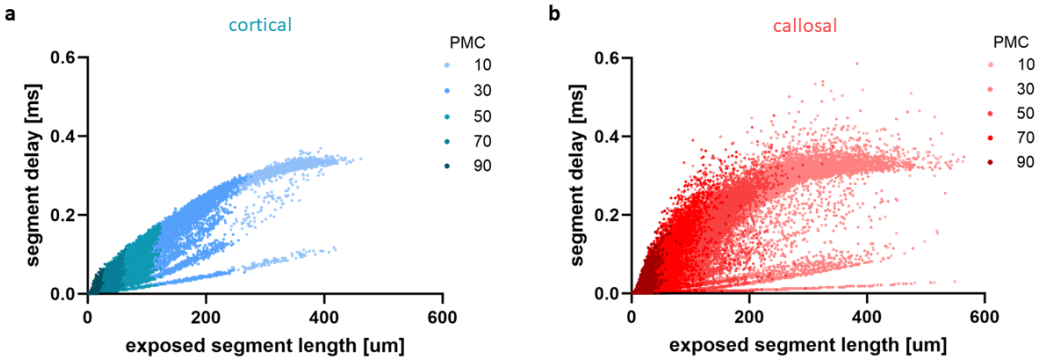

Figure 5. Non-linearity of AP propagation. a, Delays along individual exposed segments of cortical axons. **b,** Delays along individual exposed segments of callosal axons. In both panels, the intensity of the colour indicates the PMC value. As the lengths of exposed segments decrease (and hence there is more myelin along the axons) the variability of delays decreases.

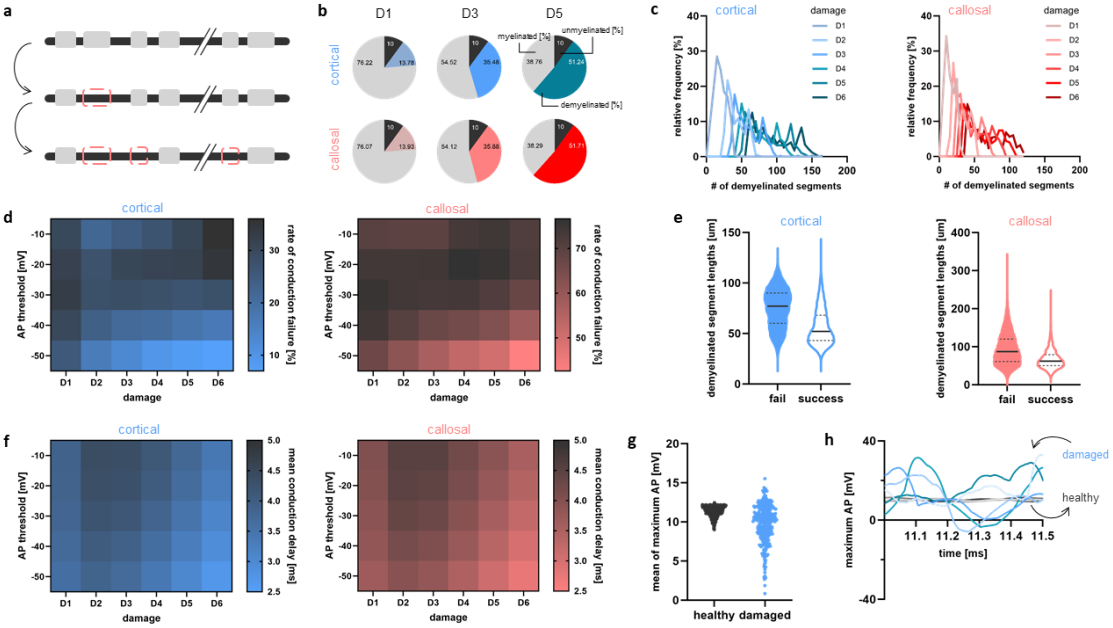

Figure 6. Vulnerability of callosal and cortical axons to demyelination. a, Schematic of the demyelination process. Healthy axons (L = 10 mm, PMC = 90%) are sequentially exposed to myelin sheath removal, in which the number of myelin sheaths is reduced by 15% each time. This process is repeated to model increasing stages (D1, . . . , D6) of damage. **b,** Pie charts show the percentage of myelinated, demyelinated and exposed areas of the axons for the 1st, 3rd and 5th stages of demyelination. **c,** Frequency distributions of the number of myelin sheaths for all stages of demyelination (D1, . . . , D6). **d,** Rate of conduction failure as a function of AP threshold and degree of damage along the axons. **e,** Violin plots of demyelinated segment lengths characterizing conduction success and conduction failure. **f,** Mean conduction delays (only of axons that successfully conduct) as a function of AP threshold and degree of damage. **g,** Mean peak amplitude values of AP for healthy (black) and damaged (blue) cortical axons in which successful conduction was observed despite damage being present. Here damage is at stage D6 and AP threshold was set to −10 mV. **h,** Representative examples of AP peak amplitude values for five damaged cortical axons and five healthy cortical axons. The curves with blue shades represent the damaged axons while those with grey shades represent healthy axons. Here damage is at stage D6 and AP threshold was set to −10 mV.

Materials and Methods

Constructing axons with heterogeneous myelination motifs

We consider a cable of fixed length L, representing a bare axon. The cumulative length of the cable covered by myelin (L_{my}) is determined by the formula $L_{my} = PMC \cdot L$, where PMC represents the percentage of myelin coverage. The remaining part of the axon constitutes the exposed length (L_{exp}), expressed as $L_{exp} = L - L_{my}$. To construct a myelinated axon, we generate myelin sheaths, each of length l^i_{my} ($i = 1, \ldots, N_{my}$), and exposed segments l^i_{exp} ($i = 1, \ldots, N_{exp}$), which are assembled in an alternating fashion. N_{my} and N_{exp} represent the total number of myelinated and exposed segments, respectively. Geometrically, the lengths L_{my} and L_{exp} correspond to the sum of individual myelinated or exposed segment lengths, as follows

$$L_{my} = \sum_{i=1}^{N_{my}} l^i_{my} \tag{1}$$

$$L_{exp} = \sum_{i=1}^{N_{exp}} l^i_{exp} \,. \tag{2}$$

The distribution of myelin sheaths with variable lengths is carried out along the cable, as detailed in subsequent analyses.

Cortical myelination motifs. To create a cortical axon we generate a set of Poisson-distributed numbers that sum to L_{my}. Each element of the set corresponds to a myelin sheath with the value of the element denoting the length of the sheath l^i_{my}. To generate this set, we first generate L_{my} points uniformly on the unit interval. In each sub-interval of length $1/N_{my}$, where N_{my} is the number of sheaths, there are on average L_{my}/N_{my} events. Hence, there will be N_{my} events in total and the Poisson rate parameter becomes $\lambda = L_{my}/N_{my}$. We subsequently check whether the following constraints are satisfied: we require that the mean value of the sheath lengths is between 40 μm and 80 μm according to [14,18], and the minimal length is no smaller than 1 μm. The lengths of exposed segments were generated in a same manner, with the additional constraint that the minimum segment length is 1 μm, a value commonly associated with a node of Ranvier [29].

Callosal myelination motifs. To create a callosal axon we adopt a similar strategy, but use a different distribution compared to the one used above. We generate a set of Gamma-distributed numbers (N_{my} in total) that sum to L_{my}. The rationale underlying the selection of the Gamma distribution stems from the irregular sheath lengths generated per oligodendrocyte within the corpus callosum observed experimentally [14].

Each element of a set following the Gamma distribution, $\Gamma(k, \theta)$, corresponds to a myelin sheath with the value of the element denoting the length of the sheath (l^i_{my}, $i = 1, \ldots, N_{my}$). The shape parameter k and the scale parameter θ vary for each axon and are sampled from the uniform distribution. We have set two constraints for the callosal axons: (i) the mean value of the sheath lengths is between 20 μm and 160 μm, and (ii) the minimal sheath length is greater or equal to 1 μm. We generate the exposed segment lengths in a same manner as with the myelin sheaths. The constraint is the same as for the cortical axons, namely that the minimal length of an exposed segment is 1 μm.

Modelling axonal conduction

The membrane potential is determined by the properties and particular structure of myelinated and exposed segments along an axon. Due to high resistance along myelin sheaths, the membrane potential travels passively there and regenerates over exposed segments characterized by higher density of ion channels. Taking these properties and the distinct myelination profiles generated above into consideration, we built a model that governs the dynamics of the membrane potential along different segments of the axon. The model is defined by the following system of partial differential equations:

$$C_c \frac{\partial u_i}{\partial t}(x,t) = \frac{a}{2r_{int}} \frac{\partial^2 u_i}{\partial x^2}(x,t) + \mathcal{I}(u_i(x,t)) \tag{3}$$

$$C_{my} \frac{\partial u_{i+1}}{\partial t}(x,t) = \frac{1}{R_c} \frac{\partial^2 u_{i+1}}{\partial x^2}(x,t) \tag{4}$$

$$u_i(p_i, t) = u_{i+1}(p_{i+1}, t) \tag{5}$$

$$\kappa_i \frac{\partial u_i}{\partial x}(p_i, t) = \kappa_{i+1} \frac{\partial u_{i+1}}{\partial x}(p_{i+1}, t) \tag{6}$$

$$\frac{\partial u}{\partial x}(0,t) = 0\,, \quad \frac{\partial u}{\partial x}(L,t) = 0 \tag{7}$$

$$u(x,0) = E_{leak} \tag{8}$$

for $i = 1, \ldots, N$, where $u_i(x,t)$, $0 < x < L$, is the membrane potential within segment i (either myelinated or exposed/unmyelinated) at time $t > 0$ and for a total of $N = N_{my} + N_{exp}$ segments.

The solution u of each differential equation involved in Eqs. (3)-(4) is the membrane potential within either an exposed segment/node of Ranvier (Eq. (3)) or a myelin sheath (Eq. (4)). We imposed continuity conditions at the paranodes (see Eqs. (5) - (6)), namely at the regions where the terminal myelin loops form septate-like junctions with the axolemma. Eq. (5) indicates that the membrane potential u is continuous across a paranodal junction while Eq. (6) assumes continuity in flux, that is, the longitudinal currents should

match at the junction. For the purpose of our analysis we have considered axons of finite length L, and hence additionally set boundary conditions at both ends of the axon. Following [56], we assume zero Neumman boundary conditions at either end (Eqs. (7)). For time $t = 0$ we set an initial condition equal to the leak reversal potential E_{leak} (Eq. (8)). We analyze the resulting governing equations and define all the parameters below.

Exposed segments/nodes of Ranvier. Equation (3) models the membrane potential u along the unmyelinated parts of the axon. This model has been introduced in [Table 5 in [44]] as a simplified version of the Hodgkin-Huxley [57] and Wang-Buzaki models [58]. It accounts for spike generation and conduction, and has been inspired by the exponential integrate-and-fire model, which simulates the rapid growth of the membrane potential. In Eq. (3), the membrane capacitance of the cable is denoted by C_c, a is the radius of the cable and r_{int} is the intracellular resistivity. Three currents are lumped together into $\mathcal{I}(u)$: the leak current (I_{leak}), the depolarizing current (I_{dep}), and the repolarizing current (I_{rep}). The leak current is given by

$$I_{leak}\left(u(x,t)\right) = g_{leak}\left(E_{leak} - u(x,t)\right), \tag{9}$$

where g_{leak} is the leak conductance and E_{leak} the leak reversal potential. Both parameters were assumed to remain constant along the axon. The depolarizing current emulates the spike initiation and is defined as

$$I_{dep}\left(u(x,t)\right) = g_{leak}\,\frac{K_{th}\,A_{th}}{1 + A_{th}\,e^{-U_{th}}} \tag{10}$$

where $U_{th} = \frac{u(x,t) - u_{th}}{K_{th}}$. The parameter u_{th} is the spike threshold, and K_{th}, A_{th} are parameters needed to control the exponential growth of the spike. When the membrane potential u reaches the preset value u_{rep}, a repolarizing current is triggered forcing the membrane potential downward to the resting state. The repolarizing current is defined as:

$$I_{rep}\left(u(x,t)\right) = G_{rep}(t)\,g_{leak}\left(E_{leak} - u(x,t)\right) \tag{11}$$

with $G_{rep}(t)$ being the repolarizing conductance for a time $t \geq T_{rep}$ (the time of activation of the repolarizing current):

$$G_{rep}(t) = A_{rep}\,\frac{t - T_{rep}}{t_{rep}}\,e^{1 - \frac{t - T_{rep}}{t_{rep}}}\,. \tag{12}$$

The parameters A_{rep} and t_{rep} are the amplitude and time constants of the repolarizing conductance, respectively.

To generate an AP, a brief external current I_{inj} is injected at a specific location at the start of the axon for a

set duration T_S:

$$I_{inj}(x,t) = \begin{cases} I_0, & x = x_0,\ t \in T_S \\ 0, & \text{elsewhere}\,. \end{cases}$$

For a thorough discussion of the model used in Eq. (3), and its advantages and disadvantages compared to the classical conduction models, we refer the reader to the original work [44]. The parameter values used here are also taken from [44] and are summarised in Table 1.

Myelin sheaths. Turning to the parts of the axon covered by myelin, we assume that the myelin sheaths have infinite resistance. Consequently, in the absence of ionic currents, the membrane potential u along a myelin sheath satisfies the diffusion equation Eq. (4) (cf. [46]). The capacitance of a myelin sheath C_{my} is defined as

$$C_{my} = \frac{2\pi\epsilon}{\ln(1/g)}$$

where ϵ is the permittivity of the myelin and g is the g-ratio, that is, the ratio of the inner-to-outer diameter of the myelinated axon. The cable resistance is given by the intracellular resistivity r_{int} over the cross-sectional area πa^2, that is,

$$R_c = \frac{r_{int}}{\pi a^2}\,.$$

Paranodal junctions. As the myelin loops bind to the axonal membrane, they form paranodal axoglial junctions at both ends of every myelin sheath. While there is a rich selection of dynamics and functions at the paranodal junctions to maintain reliable saltatory conduction [55] we exclude those details from our model. We apply the continuity conditions given in Eqs. (5)-(6) at each paranodal junction, here denoted by p_i. The diffusivities κ in Eq. (6) are defined by the diffusion coefficients of Eqs. (3)-(4). Specifically, from Eq. (3) we have $\kappa_i = \frac{1}{C_c}\frac{a}{2r_{int}}$ and from Eq. (4) $\kappa_{i+1} = \frac{1}{C_{my}}\frac{1}{R_c}$.

Net axonal conduction delays and velocities

For each segment (either myelinated or exposed/unmyelinated) along the axon, we compute the time difference between the peak of the AP at the beginning and end of the segment. This gives the conduction time delay along individual segments. We denote by τ^i_{my}, $i = 1,\ldots,N_{my}$, and τ^i_{exp}, $i = 1,\ldots,N_{exp}$, the conduction times across individual myelinated and exposed segments, respectively. Then, the net conduction

delay τ is given by the sum of these individual conduction times:

$$\tau = \sum_{i=1}^{N_{my}} \tau_{my}^{i} + \sum_{i=1}^{N_{exp}} \tau_{exp}^{i} \,. \tag{13}$$

where recall N_{my} and N_{exp} denote the number of myelinated and exposed segments, respectively. To obtain the corresponding conduction velocity (CV) v we divide the total axon length L, which is also equal to the sum of myelin sheaths and exposed segments lengths, by the conduction delay τ:

$$v = \frac{L}{\tau} \,. \tag{14}$$

Demyelination and conduction failures

We implemented a demyelination model by iteratively reducing the number of myelin sheaths by 15% in each cycle, repeated six times (D1, . . . , D6). Once a myelin sheath is damaged in any demyelination cycle, it remains impaired throughout subsequent iterations. In the event of myelin sheath damage, the segment is replaced by an excitable one with an AP threshold value ranging between −10 to −50 mV. All of these values exceed the threshold at the unaffected exposed segments/nodes of Ranvier (−60.2 mV). The threshold value serves here as a proxy for the reduced excitability of the axon, reflecting a decrease in the density of sodium ion channels; an increase in channel density corresponds to a lower AP threshold.

We compute axonal conduction delays in the same manner as in the case of healthy axons (see Eq. (13)). Specifically, the net conduction delay τ is determined by summing the conduction times across individual myelinated (τ_{my}^{i}), demyelinated (τ_{dem}^{i}) and exposed (τ_{exp}^{i}) segments, so that

$$\tau = \sum_{i=1}^{N_{my}} \tau_{my}^{i} + \sum_{i=1}^{N_{dem}} \tau_{dem}^{i} + \sum_{i=1}^{N_{exp}} \tau_{exp}^{i} \,, \tag{15}$$

where N_{my}, N_{dem} and N_{exp} denote the total number of myelinated, demyelinated and exposed segments, respectively.

We assess successful axonal conduction in K axons by counting the occurrences of superthreshold membrane potential peaks reaching the axon's endpoint. This number represents conduction successes (n_s). The number of conduction failures is $n_f = 500 - n_s$. To quantify faithful transmission, we calculate the rate of conduction failures $r_f = \frac{1}{5}\, n_f$.

Characterizing the influence of myelin distribution on AP conduction delay

The axon model used (Eq. (3)-(8)) is highly nonlinear and subjected to numerous interface conditions at the paranodal junctions. It is thus challenging to characterize mathematically the precise relationship linking myelination motifs and axonal conduction delay variability. To this end, we here employ a phenomenological approach based on axonal geometry.

Consider an axon (either cortical or callosal) of fixed length L and given PMC. Ought to the very high CV of APs across myelinated segments (due to pure diffusion, see Eq. (4)), we may assume $\tau^i_{my} \approx 0$, for all i, and express the net conduction delay given in Eq. (13) as a function of the delays along exposed segments, that is,

$$\tau \approx \sum_i^{N_{exp}} \tau^i_{exp} \,. \tag{16}$$

If the axonal CV across exposed segments is constant and independent of segment lengths (note that we break this assumption later), we may write $\tau^i_{exp} = l^i_{exp}/v_{exp}$, meaning that conduction delays scale linearly with segment length for a constant velocity v_{exp}. We further obtain a net conduction delay that depends only on the summed lengths of exposed segments,

$$\tau \approx \sum_i^{N_{exp}} \frac{l^i_{exp}}{v_{exp}} = \frac{1}{v_{exp}} \sum_i^{N_{exp}} l^i_{exp} = \frac{L_{exp}}{v_{exp}} \,. \tag{17}$$

Eq. 17 implies that if CV along exposed segments is constant, then the net conduction delay is fully independent of the distribution of myelin along the axon, relying only on PMC (that is, L_{exp}). Under this assumption, for a given axonal length and overall myelin coverage, myelination motifs are fully equivalent: they are degenerate and exhibit redundancy in terms of axonal conduction delay. In this scenario, there is no potential variability.

Given that such variability is observed in our simulations (Fig. 5), one must then consider that axonal CV along individual exposed segments is not constant, but varies instead with the distance travelled by the AP, that is,

$$v^i_{exp} = v^i_{exp,o} + \alpha(x^i_{exp} - x^i_{exp,o}) \,, \tag{18}$$

where α corresponds to a constant acceleration, $x^i_{exp} - x^i_{exp,o}$ corresponds to the distance travelled by the AP, and $v_{exp,o}$ is the initial CV of the AP at the paranodal junction. Note that setting $\alpha = 0$, the CV becomes constant and one recovers Eq. 17. Equation 18 corresponds to a first order differential equation which may

be solved trivially to obtain the conduction delay along a segment of length l^i_{exp}, that is,

$$\tau^i_{exp} = \frac{1}{\alpha} \ln \left[\frac{\alpha l^i_{exp}}{v^i_{exp,0}} + 1 \right]. \tag{19}$$

One then obtains the net conduction delay

$$\tau \approx \sum_i^{N_{exp}} \tau^i_{exp} = \frac{1}{\alpha} \sum_i^{N_{exp}} \ln \left[\frac{\alpha l^i_{exp}}{v^i_{exp,0}} + 1 \right]. \tag{20}$$

Non-linearity in axonal conduction is revealed in Eq. 20: the net conduction delay scales non-linearly with individual segment lengths, and is further distribution/motif dependent. Indeed, AP conduction time depends both on segment lengths (l^i_{exp}) as well as on the initial CV at the paranodal junction ($v_{exp,0}$), which may vary between segments. To verify the presence of such acceleration in our model, we computed numerically in Fig. 5 the conduction delay along exposed segments as a function of their individual lengths. The logarithmic increase confirms the trend of Eq. 20 and hence the presence of acceleration along exposed segments, which would otherwise remain linear.

To illustrate the influence of myelin distribution on AP propagation time variability, one may consider the exemplar and highly simplified case where initial CV does not vary between segments (that is, $v^i_{exp,0} = v_{exp,0}$). Lets further assume that exposed segments are evenly distributed, so that $l^i_{exp} = L_{exp}/N_{exp}$. With these permissive assumptions, one may simplify Eq. 20 to obtain

$$\tau \approx \frac{N_{exp}}{\alpha} \ln \left[\frac{\alpha L_{exp}}{v_{exp,0} N_{exp}} + 1 \right] \tag{21}$$

where we note that the total coverage of myelin is preserved, and only the number and length of individual exposed segments change. The susceptibility of the net conduction delay resulting from differences in the number of exposed segments N_{exp} may be observed by computing the derivative

$$\frac{\partial}{\partial N_{exp}} \tau = \frac{1}{\alpha} \ln \left[\frac{\alpha L_{exp}}{v_{exp,0} N_{exp}} + 1 \right] - \frac{L_{exp}}{N_{exp}\alpha + L_{exp} v_{exp,0}} \tag{22}$$

which is a decreasing function of N_{exp}. Consequently, increasing the number of exposed segments, or equivalently decreasing their individual lengths, decreases the variability of the net conduction delay. This analysis supports the findings of Fig. 5, in which cortical axons display smaller variability compared to callosal axons. Furthermore, in the limit of large N_{exp} where exposed segments become infinitesimally small - as commonly assumed for exposed segments - variability is quenched and the net conduction delay becomes

linearly proportional to axon length.

Tables

Table 1. List of model variables and parameters

Symbol	Definition	Value
K	total number of axons	500
L	axonal length	variable
L_{my}	myelinated axon length	variable
L_{exp}	exposed axon length	variable
l_{my}	length of a myelin sheath	variable
N_{my}	number of myelin sheaths	variable
l_{exp}	length of an exposed segment	variable
N_{exp}	number of exposed segments	variable
N	total number of segments	variable
λ	Poisson parameter	variable
k	shape parameter	variable
θ	scale parameter	variable
C_c	cable membrane capacitance	$3.5\,\mu F/cm^2$
a	cable radius	$2\mu m$
r_{int}	intracellular resistivity	$100\,MOhm \cdot \mu m$
E_{leak}	leak reversal potential	-68.3 mV
g_{leak}	leak conductance	$10\,mS/cm^2$
K_{th}	slope factor	$3.5\,mV$
A_{th}	ceiling factor	520
u_{th}	spike threshold	$-60.2\,mV$
u_{rep}	starting voltage of repolarizing current	$10\,mV$
t_{rep}	time constant of repolarizing conductance	$1\,ms$
A_{rep}	amplitude constant of the repolarizing conductance	90
I_0	amplitude of the injected current	$0.01\,nA$
ϵ	dielectric constant	$1.4 \cdot 10^{-11}\,F/m$
g	g-ratio	0.6

Data Availability

The authors will make the data available upon publication.

Code Availability

The authors will make the code available upon publication.

Acknowledgements

We thank the National Research Council of Canada (NSERC GRANT RGPIN-2017-06662) as well as the Canadian Institute of Health Research (CIHR GRANT NO PJT-156164) for funding.

Author Contributions Statement

AT and JL designed the study. AT and JL performed the mathematical derivations and simulations. AT and JL wrote the manuscript.

Declaration of Interests

None to declare.

References

[1] Bradl M, Lassmann H. Oligodendrocytes: biology and pathology. *Acta Neuropathol.*, 119(1):37-53 (2010).

[2] Simons M, Nave KA. Oligodendrocytes: Myelination and Axonal Support. *Cold Spring Harb Perspect Biol.*, 22;8(1):a020479 (2015)

[3] Steadman PE et al. Disruption of oligodendrogenesis impairs memory consolidation in adult mice. *Neuron* 105, 150–164.e6 (2020).

[4] Pan S, Mayoral SR, Choi HS, Chan JR & Kheirbek MA. Preservation of a remote fear memory requires new myelin formation. *Nat. Neurosci* 23, 487–499 (2020).

[5] Bengtsson, S.L. et al. Extensive piano practicing has regionally specific effects on white matter development. *Nat. Neurosci.* 8, 1148–1150 (2005).

[6] Xin W, Chan JR. Myelin plasticity: sculpting circuits in learning and memory. *Nat Rev Neurosci.*;21(12):682-694 (2020).

[7] McKenzie IA et al. Motor skill learning requires active central myelination. *Science* 346, 318–322 (2014).

[8] Mabbott, D.J. et al. White matter growth as a mechanism of cognitive development in children. *Neuroimage* 33, 936–946 (2006).

[9] Nagy, Z. et al. Maturation of white matter is associated with the development of cognitive functions during childhood. *J. Cogn. Neurosci.* 16, 1227–1233 (2004).

[10] Pujol, J. et al. Myelination of language-related areas in the developing brain. *Neurology* 66, 339–343 (2006).

[11] Ian D. Duncan, Abigail B. Radcliff, Inherited and acquired disorders of myelin: The underlying myelin pathology, *Experimental Neurology*, Volume 283, Part B, Pages 452-475 (2016).

[12] Takahashi N, Sakurai T, Davis KL, Buxbaum JD. Linking oligodendrocyte and myelin dysfunction to neurocircuitry abnormalities in schizophrenia. *Prog Neurobiol.*;93(1):13-24 (2011).

[13] R. Douglas Fields, White matter in learning, cognition and psychiatric disorders, *Trends in Neurosciences*, Volume 31, Issue 7, Pages 361-370, (2008).

[14] Chong SY, Rosenberg SS, Fancy SP, Zhao C, et al. Neurite outgrowth inhibitor Nogo-A establishes spatial segregation and extent of oligodendrocyte myelination. *Proc Natl Acad Sci U S A*. 24;109(4):1299-304 (2012).

[15] Tomassy GS, Berger DR, Chen HH, Kasthuri N, Hayworth KJ, Vercelli A, Seung HS, Lichtman JW, Arlotta P. Distinct profiles of myelin distribution along single axons of pyramidal neurons in the neocortex. *Science*; 344(6181):319-24 (2014).

[16] Micheva KD, Wolman D, Mensh BD, Pax E, Buchanan J, Smith SJ, Bock DD. A large fraction of neocortical myelin ensheathes axons of local inhibitory neurons. *Elife*; 5:e15784 (2016).

[17] Hill RA, Li AM, Grutzendler J. Lifelong cortical myelin plasticity and age-related degeneration in the live mammalian brain. *Nat Neurosci.*;21(5):683-695 (2018).

[18] Call, C.L., Bergles, D.E. Cortical neurons exhibit diverse myelination patterns that scale between mouse brain regions and regenerate after demyelination. *Nat Commun* 12, 4767 (2021).

[19] Auer F, Vagionitis S, Czopka T. Evidence for Myelin Sheath Remodeling in the CNS Revealed by In Vivo Imaging. *Curr Biol.*;28(4):549-559.e3 (2018).

[20] Stedehouder J, Brizee D, Slotman JA, Pascual-Garcia M, Leyrer ML, Bouwen BL, Dirven CM, Gao Z, Berson DM, Houtsmuller AB, Kushner SA. Local axonal morphology guides the topography of interneuron myelination in mouse and human neocortex. *Elife.*;8:e48615 (2019).

[21] Bakiri, Y., Karadottir, R., Cossell, L. & Attwell, D. Morphological and electrical properties of oligodendrocytes in the white matter of the corpus callosum and cerebellum. *J. Physiol.* 589, 559–573 (2011).

[22] Sturrock, R. R. Myelination of the mouse corpus callosum. *Neuropathol. Appl Neurobiol.* 6, 415–420 (1980).

[23] Ford MC, Alexandrova O, Cossell L, Stange-Marten A, Sinclair J, Kopp-Scheinpflug C, Pecka M, Attwell D, Grothe B. Tuning of Ranvier node and internode properties in myelinated axons to adjust action potential timing. *Nat Commun.*;6:8073 (2015).

[24] Benamer N, Vidal M, Balia M, Angulo MC. Myelination of parvalbumin interneurons shapes the function of cortical sensory inhibitory circuits. *Nat Commun.*;11(1):5151 (2020).

[25] Mount, C. W. & Monje, M. Wrapped to adapt: experience-dependent myelination. *Neuron* 95, 743–756 (2017).

[26] Gibson, E. M. et al. Neuronal activity promotes oligodendrogenesis and adaptive myelination in the mammalian brain. *Science* 344, 1252304 (2014).

[27] Baraban, M., Koudelka, S. & Lyons, D. A. Ca2+ activity signatures of myelin sheath formation and growth in vivo. *Nat. Neurosci.* 21, 19–23 (2018).

[28] Krasnow, A. M., Ford, M. C., Valdivia, L. E., Wilson, S. W. & Attwell, D. Regulation of developing myelin sheath elongation by oligodendrocyte calcium transients in vivo. *Nat. Neurosci.* 21, 24–28 (2018).

[29] Arancibia-Cárcamo IL, Ford MC, Cossell L, Ishida K, Tohyama K, Attwell D. Node of Ranvier length as a potential regulator of myelinated axon conduction speed. *Elife.*;6:e23329 (2017).

[30] Koskinen MK, Laine M, Abdollahzadeh A, Gigliotta A, Mazzini G, Journée S, Alenius V, Trontti K, Tohka J, Hyytiä P, Sierra A, Hovatta I. Node of Ranvier remodeling in chronic psychosocial stress and anxiety. *Neuropsychopharmacology.* ;48(10):1532-1540 (2023).

[31] Arancibia-Carcamo IL, Attwell D. The node of Ranvier in CNS pathology. *Acta Neuropathol.*;128(2):161-75 (2014).

[32] Dolma, Dolma S, Joshi A. The Node of Ranvier as an Interface for Axo-Glial Interactions: Perturbation of Axo-Glial Interactions in Various Neurological Disorders. *J Neuroimmune Pharmacol.* ;18(1-2):215-234 (2023).

[33] Freeman SA, Desmazières A, Fricker D, Lubetzki C, Sol-Foulon N. Mechanisms of sodium channel clustering and its influence on axonal impulse conduction. *Cell Mol Life Sci.* ;73(4):723-35 (2016).

[34] FitzHugh R., Computation of impulse initiation and saltatory conduction in a myelinated nerve fibre. *Biophys J.*; 26:11–21 (1962).

[35] Goldman L, Albus JS. Computation of impulse conduction in myelinated fibers; theoretical basis of the velocity-diameter relation. *Biophys J.*; 8:596–607 (1968).

[36] Basser P. Cable equation for a myelinated axon derived from its microstructure. *Med Biol Eng Comput.*; 31(1):87–92 (1993).

[37] Nygren A, Halter J. A general approach to modeling conduction and concentration dynamics in excitable cells of concentric cylindrical geometry. *J Theor Biol.*;199(3):329–58 (1999).

[38] McIntyre CC, Richardson AG, Grill WM. Modeling the excitability of mammalian nerve fibers: Influence of afterpotentials on the recovery cycle. *J Neurophysiol.*; 87(2):995–1006 (2002).

[39] Gow A, Devaux J. A model of tight junction function in central nervous system myelinated axons. *Neuron Glia Biol.*; 4(4):307–317 (2008).

[40] Schmidt H, Knösche TR. Action potential propagation and synchronisation in myelinated axons. *PLoS Comput Biol.*; 15(10):e1007004 (2019).

[41] Naud R, Longtin A. Linking demyelination to compound action potential dispersion with a spike-diffuse-spike approach. *J Math Neurosci.*; 9(1):3 (2019).

[42] Scurfield A, Latimer DC. A computational study of the impact of inhomogeneous internodal lengths on conduction velocity in myelinated neurons. *PLoS One.*; 3(1):e0191106 (2018).

[43] Babbs CF, Shi R. Subtle paranodal injury slows impulse conduction in a mathematical model of myelinated axons. *PLoS One.*; 8(7):e67767 (2013).

[44] Ashida G, Nogueira W. Spike-Conducting Integrate-and-Fire Model. *eNeuro.* Sep 7;5(4):ENEURO.0112-18.2018 (2018).

[45] Grindrod P, Sleeman BD. A model of a myelinated nerve axon: threshold behaviour and propagation. *J Math Biol.*; 23(1):119-35 (1985).

[46] Dayan, P., Abbott, L.F.: Theoretical Neuroscience. *MIT Press*, Cambdridge (2005)

[47] de Faria, O., Pivonkova, H., Varga, B. et al. Periods of synchronized myelin changes shape brain function and plasticity. *Nat Neurosci* 24, 1508–1521 (2021).

[48] Schauf CL, Davis FA. Impulse conduction in multiple sclerosis: a theoretical basis for modification by temperature and pharmacological agents. *J Neurol Neurosurg Psychiatry.*; 37(2):152-61 (1974).

[49] Tien NW, Kerschensteiner D. Homeostatic plasticity in neural development. *Neural Dev.*; 13(1):9 (2018).

[50] Basu K, Appukuttan S, Manchanda R, Sik A. Difference in axon diameter and myelin thickness between excitatory and inhibitory callosally projecting axons in mice. *Cereb Cortex.*; 33(7):4101-4115 (2023).

[51] Wu LM, Williams A, Delaney A, Sherman DL, Brophy PJ. Increasing internodal distance in myelinated nerves accelerates nerve conduction to a flat maximum. *Curr Biol.*; 22(20):1957-61 (2012).

[52] Salami, M., Itami, C., Tsumoto, T. & Kimura, F. Change of conduction velocity by regional myelination yields constant latency irrespective of distance between thalamus and cortex. *Proc. Natl Acad. Sci. USA* 100, 6174–6179 (2003).

[53] Kimura F, Itami C. Myelination and isochronicity in neural networks. *Front Neuroanat.* ;3:12 (2009).

[54] Bacmeister, C.M., Huang, R., Osso, L.A. et al. Motor learning drives dynamic patterns of intermittent myelination on learning-activated axons. *Nat Neurosci* 25, 1300–1313 (2022).

[55] Rosenbluth J. Multiple functions of the paranodal junction of myelinated nerve fibers. *J Neurosci Res.*;87(15):3250-8 (2009).

[56] Rall W. Time constants and electrotonic length of membrane cylinders and neurons. *Biophys J.*; 9(12):1483-508 (1969).

[57] Hodgkin AL, Huxley AF. A quantitative description of membrane current and its application to conduction and excitation in nerve. *J Physiol.*; 117(4):500-44 (1952).

[58] Wang XJ, Buzsáki G. Gamma oscillation by synaptic inhibition in a hippocampal interneuronal network model. *J Neurosci.* ;16(20):6402-13 (1996).

[59] Coggan JS, Prescott SA, Bartol TM, Sejnowski TJ. Imbalance of ionic conductances contributes to diverse symptoms of demyelination. *Proc Natl Acad Sci USA*;107(48):20602-9 (2010).

[60] Talidou, A., Burchard, A. & Sigal, I.M. Near-Pulse Solutions of the FitzHugh–Nagumo Equations on Cylindrical Surfaces. *J Nonlinear Sci* 31, 57 (2021).

[61] biorender.com

[62] Prins M, Schul E, Geurts J, van der Valk P, Drukarch B, van Dam AM. Pathological differences between white and grey matter multiple sclerosis lesions. *Ann N Y Acad Sci.*; 1351:99-113 (2015).

[63] Lie IA, Weeda MM, Mattiesing RM, Mol MAE, Pouwels PJW, Barkhof F, Torkildsen Ø, Bø L, Myhr KM, Vrenken H. Relationship Between White Matter Lesions and Gray Matter Atrophy in Multiple Sclerosis: A Systematic Review. *Neurology.*; 98(15):e1562-e1573 (2022).

[64] Geurts JJ, Barkhof F. Grey matter pathology in multiple sclerosis. *Lancet Neurol.*; 7(9):841-51 (2008).